Conti, R. & Caputo, G. (2019). *Géotechnique* **69**, No. 5, 377–390 [https://doi.org/10.1680/jgeot.17.P.033]

A numerical and theoretical study on the seismic behaviour of yielding cantilever walls

R. CONTI* and G. CAPUTO†

This paper provides an interpretation of the dynamic behaviour of yielding cantilever walls, regarding which open issues still remain about the applicability of the Mononobe–Okabe theory and the possible occurrence of phase shift between the maximum soil thrust and the inertia forces into the system, which both affect the seismic design of these structures. To this end, the predictions of a pseudostatic limit equilibrium/analysis model are combined with the results of an extensive numerical study, with both pseudostatic and dynamic analyses performed under real earthquakes and simple input motions. Numerical outcomes show that the maximum soil thrust on the stem and the maximum bending moment are always in phase and occur when the inertia forces are away from the backfill. The proposed model provides a good prediction of the maximum internal forces induced by the earthquake. It is shown that the possible activation of plastic mechanisms within the system, in the form of either sliding or bearing failure, makes the critical acceleration a key ingredient for the seismic design of cantilever walls, controlling both the maximum internal forces and the magnitude and trend of final displacements. Numerical and theoretical findings are used to provide suggestions for the seismic design of cantilever walls.

KEYWORDS: bearing capacity; earth pressure; earthquakes; limit equilibrium methods; numerical modelling; retaining walls

INTRODUCTION

Reinforced concrete cantilever walls are widely used in design practice as an alternative to gravity walls, combining the flexural behaviour of the structural elements with the stabilising action of the soil mass above the footing slab. In contrast to other types of retaining structures, such as basement walls or bridge abutments, yielding cantilever walls do not have kinematic constraints and their movements permit the development of active limit conditions in the retained soil, both under static and dynamic conditions.

Field observations during recent earthquakes (Verdugo *et al*., 2012; Wagner & Sitar, 2016) have shown that the overall performance of retaining structures is generally satisfactory and that the majority of failures involved either waterfront structures, due to the onset of liquefaction phenomena within the saturated backfill, or structures on slopes. Moreover, observations on the behaviour of yielding cantilever walls during the Kobe earthquake in 1995 have revealed significant tilting of the walls, in addition to sliding, reflecting the activation of a bearing capacity failure under dynamic loading (Anderson *et al*., 2008).

Although the static behaviour of cantilever walls is nowadays well understood, both from an experimental and a theoretical point of view, there are still open issues in the scientific literature regarding their seismic behaviour. Specifically, two topics are of major concern, namely: (*a*) the applicability of the Mononobe–Okabe (MO) theory in computing the dynamic soil thrust and (*b*) the possible phase shift between the maximum value of the soil thrust and the inertia forces into the wall–soil system, as this affects the computed maximum internal forces in the structural elements.

According to Psarropoulos *et al*. (2005), the MO method provides a realistic interpretation of the behaviour exhibited by yielding walls in small-scale tests. However, while many authors agree that the dynamic pressure behind the wall increases linearly with depth (Mikola *et al*., 2016), centrifuge data have shown that the MO method can lead to a significant over-prediction of the soil thrust acting on the vertical stem, particularly for high values of free-field accelerations (Koseki *et al*., 2003; Wagner & Sitar, 2016). In particular, Koseki *et al*. (2003) noticed that this observation is associated with a substantial reduction of the soil-wedge acceleration with respect to the input one. An attempt to solve the apparent mismatch between observations and MO predictions was recently proposed by Brandenberg *et al*. (2015), who applied the general framework of kinematic soil–structure interaction to the interpretation of the dynamic behaviour of cantilever walls.

As far as the second issue is concerned, similarly to what is observed for gravity retaining walls (Athanasopoulos-Zekkos *et al*., 2013; Conti *et al*., 2013), Green *et al*. (2008) and Kloukinas *et al*. (2015) claimed that the soil thrust maximising the internal forces on the vertical stem develops when the wall is moving towards the backfill, causing the retained soil to approach passive limit state conditions and the earth pressure distribution to be different from, and certainly larger than, the active limit value. However, based on the results from centrifuge tests on small-scale cantilever walls, Al Atik & Sitar (2010) concluded that the maximum structural bending moments occur when the inertia forces in the soil–wall system act in the active direction and the earth pressure is close to its static value. While both these observations suggest the possible occurrence of a phase shift between maximum (active) inertia forces into the system, maximum soil dynamic thrust and maximum bending moments, a reliable interpretation of the actual physical

Manuscript received 9 February 2017; revised manuscript accepted 8 June 2018. Published online ahead of print 9 July 2018.
Discussion on this paper closes on 1 October 2019, for further details see p. ii.
* Niccolò Cusano University, Rome, Italy (Orcid:0000-0001-7255-4537).
† Niccolò Cusano University, Rome, Italy.

phenomenon seems still to be lacking, thus leading to controversial recommendations for the structural design of such structures under seismic conditions (Aashto, 2012).

This work examines the dynamic behaviour of yielding cantilever walls, combining a theoretical pseudostatic model with the results of an extensive numerical parametric study. Specifically, plane-strain analyses were carried out on a pair of cantilever walls, considering different wall geometries and soil profiles, subjected to real earthquakes. The input signals were chosen to represent a significant range of dominant frequencies (governing possible local amplification and resonance phenomena) and peak accelerations (governing non-linearity and irreversibility of soil behaviour).

The goal of this study is threefold: (*a*) to offer a physical insight into the relevant factors affecting the seismic behaviour of yielding cantilever walls; (*b*) to introduce a new key to interpretation of the observed behaviour, based on the theoretical framework provided by the critical acceleration concept (Conti *et al*., 2013); (*c*) to provide suggestions for the seismic design, both geotechnical and structural, of these structures.

The authors consider only dry cohesionless backfill and ignore any possible reduction of soil strength due to softening behaviour or pore pressure build-up.

THEORETICAL BACKGROUND AND CRITICAL ACCELERATION

The seismic design of yielding cantilever walls is usually carried out with a pseudostatic approach, that is converting the seismic acceleration acting on the system to an equivalent constant pseudostatic coefficient and computing the resulting soil thrust using either limit equilibrium methods or limit analysis. Despite the simplifying assumption on the seismic action, the pseudostatic approach has been proven to provide valuable information on the behaviour of yielding retaining structures during earthquakes, both for embedded (Conti *et al*., 2012, 2014) and gravity (Conti *et al*., 2013; Masini *et al*., 2015) walls, where the onset of plastic mechanisms within the soil–structure system makes the dynamic interaction problem a strength-driven rather than a deformability-driven problem. Indeed, the elastic solutions provided in the literature for the computation of the dynamic soil thrust (Veletsos & Younan, 1997; Brandenberg *et al*., 2015) are of little applicability in this context, as they do not take into account the strength of the system.

Figure 1(a) shows the typical layout for a cantilever wall (height H, base width B, heel width d, toe width a, embedment depth D), retaining a cohesionless backfill (unit weight γ, friction angle ϕ') and resting on a cohesive-frictional soil (unit weight γ_f, friction angle ϕ'_f, cohesion c'_f, undrained shear strength c_{uf}). Fig. 1(b) shows the forces acting on the soil–wall system under the horizontal ($a_h = k_h \boldsymbol{g}$) and vertical ($a_v = k_v \boldsymbol{g}$) pseudostatic accelerations, the latter usually being neglected as of minor relevance in the seismic design of gravity walls (Gazetas *et al*., 2009). Both the dynamic active soil thrust acting on the vertical plane AV, S_{AV}, its inclination on the horizontal, δ_S, and the inclination of the two failure surfaces, ω_α and ω_β, were derived by Kloukinas & Mylonakis (2011) and Evangelista *et al*. (2010), as a function of the pseudostatic coefficient k_h, in the realm of a rigorous stress plasticity theory (see Appendix).

On the one hand, the external stability of the system against the possible onset of plastic mechanisms (geotechnical design) must be assessed under the outlined system of external forces, giving rise to an inclined and eccentric resultant at the foundation level (Fig. 1(c)). In this context, the yield acceleration, a_y, can be computed for any of the possible collapse mechanisms of the wall (overturning, $a_{y,ROT}$; sliding over the base, $a_{y,SLID}$; bearing capacity failure of the foundation soil, $a_{y,QLIM}$), as the value of the pseudostatic acceleration corresponding to which the strength of the system is fully mobilised or, equivalently, the driving actions match the resisting ones. Therefore, defining the critical

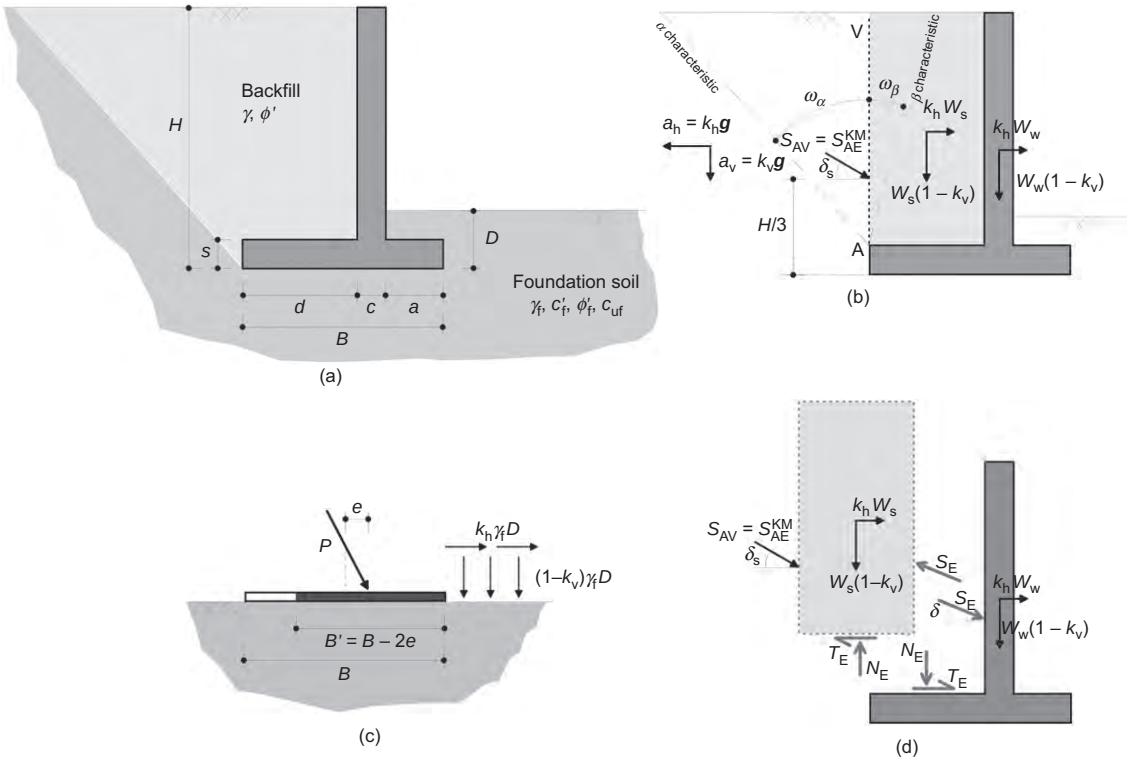

Fig. 1. Cantilever walls: (a) typical layout; (b) system of pseudostatic external forces; (c) assessment of the external stability; (d) assessment of the internal stability

Table 1. Approximate theoretical solutions for the horizontal force acting on the vertical stem

Solution	$S_{E,h}$	M_{max}	$\sigma_h(z)$
S1(k_h)	$S^{KM}_{AE,h}(k_h) + k_h W_s$	$S^{KM}_{AE,h}(k_h)\frac{H}{3} + k_h\left(W_{w,stem} + W_s\right)\frac{H}{2}$	$K^{KM}_{AE,h}\gamma z + k_h\gamma d$
S2(k_h)	$S^{MO}_{AE,h}(k_h)$	$S^{MO}_{AE,h}(k_h)\frac{H}{3} + k_h W_{w,stem}\frac{H}{2}$	$K^{MO}_{AE,h}\gamma z$

acceleration of the wall, a_c, as the one corresponding to which a plastic mechanism is activated within the soil–structure system and the wall starts to experience permanent displacements, it follows that

$$a_c = \min\left\{a_{y,SLID}, a_{y,QLIM}\right\}$$

where $a_{y,ROT}$ has been omitted, as this is always significantly larger than the others. $a_{y,SLID}$ can be computed using the method proposed by Richards & Elms (1979), while upper-bound solutions for the seismic bearing capacity of shallow foundations can be used to compute $a_{y,QLIM}$ (Conti, 2018).

On the other hand, when dealing with the internal stability of the vertical stem (structural design), the soil thrust effectively acting on its back (S_E) must be taken into account, resulting from the dynamic interaction (both inertial and kinematic) between the soil volume above the heel and the wall (Fig. 1(d)). Table 1 reports two possible approximate solutions for $S_{E,h}$, that will both be referred to in the following interpretation of numerical results. In the first case (S1), it is assumed that no shear stresses develop at the contact between the heel and the soil above it ($T_E = 0$), and hence the soil thrust S_{AV} and the inertia forces $k_h W_s$ are entirely transferred to the vertical stem. The second solution (S2), instead, implicitly assumes that even the soil volume above the heel is in active limit state conditions and that the presence of the horizontal stem does not alter the resulting soil thrust. In this condition, S_E can be computed using the MO theory.

PROBLEM LAYOUT AND ANALYSIS PROCEDURE

Figure 2 shows the problem layouts analysed in this work. Three different geometries were considered for the wall (W1, W2, W3), varying only in the length, a, of the toe ($H = 5$ m, $d = 2{\cdot}6$ m, $c = 0{\cdot}4$ m, $s = 0{\cdot}5$ m, $\gamma_{cls} = 25$ kN/m^3), while two different soil deposits were chosen, including a cohesionless (soil number 2: $c' = 0$ kPa, $\phi' = 30$ kPa) and a cohesive (soil number 3: $c_u = 80$ kPa, $\phi_u = 0°$) soil layer immediately beneath the foundation, with drained (D) and undrained (UD) behaviour, respectively. In both cases the cohesionless backfill (soil number 1) has a friction angle of $\phi' = 40°$, the total depth of the soil deposit is 30 m, and a uniform unit weight of $\gamma = 20$ kN/m^3 was chosen for all of the layers. As far as the mechanical properties of the interface between the wall and its base are concerned, a pure frictional ($\phi_b = 30°$) and a pure adhesive ($c_w = 50$ kPa) contact was assumed in the drained and undrained case, respectively.

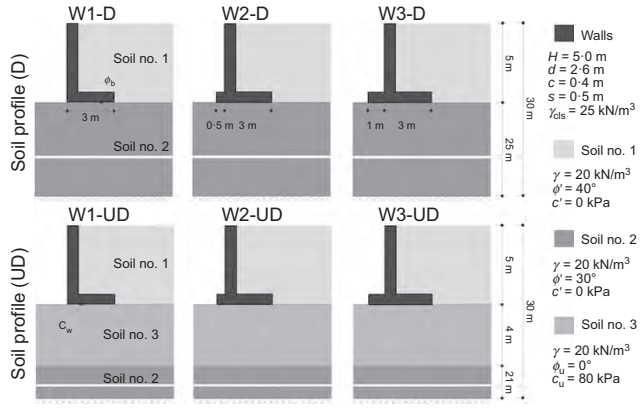

Fig. 2. Problem layouts considered in the numerical study

For the six layouts outlined, Table 2 reports the static global safety factors for the sliding (SF_{SLID}) and bearing failure (SF_{QLIM}) mechanisms, together with the theoretical values of the yield accelerations. In drained conditions the critical mechanism is always the bearing capacity failure. Moreover, the critical accelerations computed for the drained case are significantly smaller than those corresponding to the undrained behaviour of the supporting soil.

Numerical model

Plane-strain analyses were carried out on a pair of cantilever walls, using the finite-difference code Flac v.5 (Itasca, 2005). Fig. 3 shows a detail of the mesh adopted in the numerical analyses. Points N_{TOP}, N_{MID}, N_{BOT}, N_B and N_{ff} – respectively at the top, mid-height and bottom of the wall, just outside the soil wedge and in free-field conditions – will be considered in the discussion of results.

The retaining walls were modelled as elastic beams (density $\rho = 2{\cdot}55$ Mg/m^3, Young's modulus $E = 40$ GPa, and Poisson ratio $\nu = 0{\cdot}15$), connected to the grid nodes using elastic–perfectly plastic interfaces with a very large normal and tangential stiffness ($k_n = k_s = 2 \times 10^7$ kN/m). Table 3 summarises the strength properties adopted for the interfaces.

The soil was modelled as an elastic–perfectly plastic material with a Mohr–Coulomb failure criterion and a non-associated flow rule, with zero dilatancy. Table 4 summarises the main physical and mechanical properties adopted in the numerical analyses. The small-strain shear modulus, G_0, is a function of the mean effective stress, p', with typical expressions for sands (soil number 1 and number 2) and medium plasticity clays (soil number 3).

During the dynamic stage, a non-linear and dissipative behaviour was introduced for stress paths within the yield surface through a hysteretic model described in detail in

Table 2. Problem layouts: static safety factors and yield accelerations

Wall		Static safety factors		Yield accelerations: g	
Type	Soil profile	SF_{SLID}	SF_{QLIM}	$a_{y,SLID}$	$a_{y,QLIM}$
W1	D	3·4	2·2	0·41	0·06
W2	D	3·4	4·3	0·41	0·15
W3	D	3·5	5·6	0·41	0·21
W1	UD	2·8	2·7	0·21	0·18
W2	UD	3·2	3·9	0·25	0·28
W3	UD	3·7	4·4	0·29	0·36

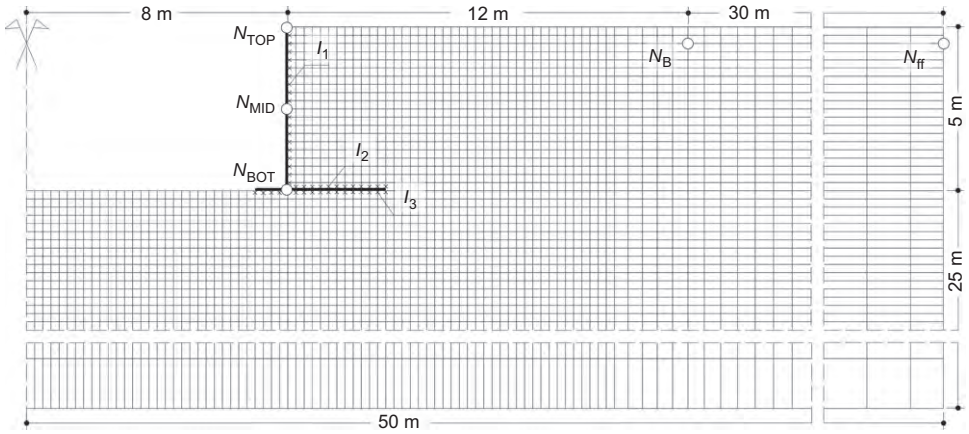

Fig. 3. Detail of the finite-difference grid adopted in the numerical analyses

Table 3. Strength parameters of the soil–wall interfaces

Interface	Analysis	Friction angle: degrees	Cohesion: kPa
I1	D/UD	20	0
I2	D/UD	30	0
I3	D	30	0
I3	UD	0	50

Table 4. Parameters of soil constitutive models

Soil	γ: kN/m^3	ϕ: degrees	c: kPa	v	G_0: MPa
Number 1	20	40	0	0·2	$10{\cdot}0 \times (p')^{0{\cdot}5}$
Number 2	20	30	0	0·2	$10{\cdot}0 \times (p')^{0{\cdot}5}$
Number 3	20	0	80	0·2	$1{\cdot}0 \times (p')^{0{\cdot}8}$

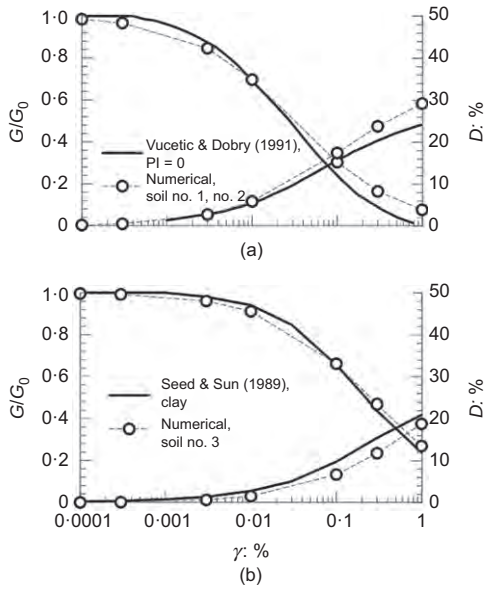

Fig. 4. Modulus decay and damping ratio curves for: (a) sand; (b) clay

Conti *et al*. (2014). Fig. 4 shows the modulus decay curves and the equivalent damping ratio provided by the adopted model for the three layers, together with those suggested by Vucetic & Dobry (1991) and Seed & Sun (1989) for cohesionless soils and clay, respectively.

Procedure for analysis

After initialising the geostatic stress state in the foundation soil elements, the cantilever walls were installed and the backfill elements were activated in five successive steps. During this stage, standard boundary conditions were applied to the model, that is: zero horizontal displacements along the lateral boundaries and fixed nodes at the base of the grid.

After the initial static stage, both pseudostatic and dynamic analyses were carried out. In the pseudostatic analyses, a uniform body force, defined as a fraction k_h of the gravitational acceleration, was applied in the horizontal direction, and the pseudostatic coefficient k_h was gradually increased until static equilibrium became no longer possible and a plastic mechanism appeared within the soil–wall system (Masini *et al*., 2015).

In the dynamic analyses, the selected acceleration–time histories were applied to the bottom nodes of the grid, together with a zero velocity in the vertical direction, while standard periodic constraints were applied to the nodes on the lateral boundaries of the grid. A small Rayleigh viscous damping ($D = 1\%$ at $f = 2{\cdot}5$ Hz) was adopted to remove the high-frequency noise deriving from the numerical integration, but not otherwise affecting the results.

Seismic input

Figure 5 shows the eight acceleration–time histories applied in the dynamic analyses, all registered on rock outcrop during real earthquakes, while Table 5 summarises the corresponding ground motion parameters, that is: peak ground acceleration (PGA), velocity (PGV) and displacement (PGD); dominant frequency, f_d; mean frequency, f_m; Arias intensity, I_a; and duration $T_{5\text{-}95}$. All the recorded signals were baseline-corrected and low-pass-filtered at 10 Hz for compatibility with the dimension of the grid elements. Moreover, simple Morlet wavelet excitations were applied, with a nominal frequency of 0·8 Hz, scaled at maximum accelerations ranging from 0·05$\boldsymbol{g}$ to 0·35$\boldsymbol{g}$.

Summarising, in total, 78 dynamic analyses were carried out, taking into account different wall geometries (W1, W2, W3), different soil conditions (D, UD) and different seismic inputs. In the following, accelerations are positive rightwards and the horizontal displacements of the walls are positive if away from the backfill.

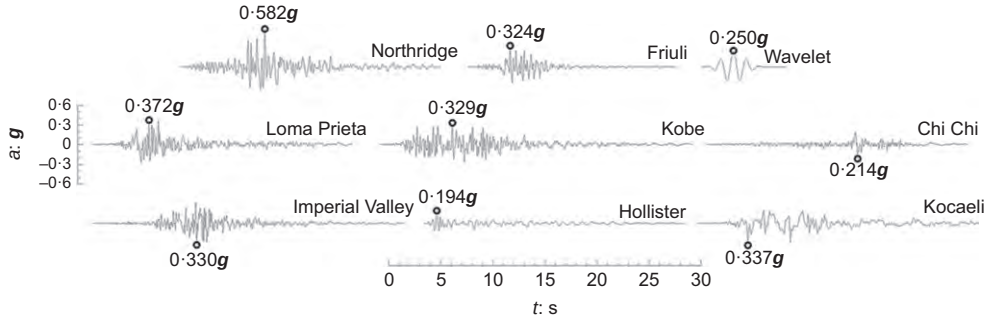

Fig. 5. Seismic inputs

Table 5. Ground motion parameters of the input earthquakes

Earthquake	PGA: g	PGV: m/s	PGD: m	f_d: Hz	f_m: Hz	I_a: m/s	$T_{5\text{-}95}$: s
Northridge – USA (1994)	0·582	0·514	0·108	1·28	2·71	2·70	9·0
Loma Prieta – USA (1989)	0·372	0·443	0·183	0·72	3·29	1·26	10·4
Kobe – Japan (1995)	0·329	0·281	0·116	0·58	3·69	1·65	11·8
Imperial Valley – USA (1979)	0·330	0·307	0·162	7·15	3·80	1·21	8·4
Hollister – Usa (1961)	0·194	0·120	0·044	0·88	2·22	0·25	14·6
Chi Chi – Taiwan (1999)	0·214	0·198	0·180	0·74	3·19	0·26	11·7
Friuli – Italy (1976)	0·324	0·222	0·042	3·78	3·28	0·76	4·2
Kocaeli – Turkey (1999)	0·337	0·609	0·502	0·78	1·45	1·31	14·7

PSEUDOSTATIC ANALYSES

Plastic mechanisms

The pseudostatic numerical analyses permit investigation of both the shape of the plastic mechanism induced in the soil–wall system by a uniform horizontal acceleration field and the value of the critical pseudostatic coefficient, k_c, corresponding to which the mechanism is activated. Fig. 6 shows, for the six layouts considered in this study, the contours of shear strains computed in critical conditions, together with the critical failure mechanisms predicted by theoretical methods (as pointed out by Masini *et al.* (2015) the actual values of the shear strain are not relevant in this case).

In drained conditions the plastic mechanism involves the development of shear deformations within the supporting soil, related to the bearing failure of the foundation, eventually leading to both sliding and rotation of the wall. In undrained conditions, instead, the critical mechanism corresponds essentially to a pure sliding of the wall along its base. For the sole L-shaped wall (W1), a very shallow failure surface is observed, both numerically and theoretically, indicating that in this case the driving moment affects the plastic mechanism.

Numerical and theoretical results show some discrepancies in terms of the shape of the slip surfaces, essentially due to the non-associated flow rule assumed for the cohesionless soils and to the combined effect of sliding and tilting of the wall, the latter inducing a non-uniform deformation field within the backfill. Nonetheless, the predicted values of k_c are in very good agreement, both in drained and undrained conditions.

Figure 6 also indicates a progressive rotation of the characteristic lines within the backfill with increasing the critical pseudostatic coefficient, as predicted by the stress plasticity theory. This observation confirms the assumption that, moving from static to dynamic conditions, the wall interface has a minor influence on the soil stress state at the surface AV, at least for standard lengths of the internal heel,

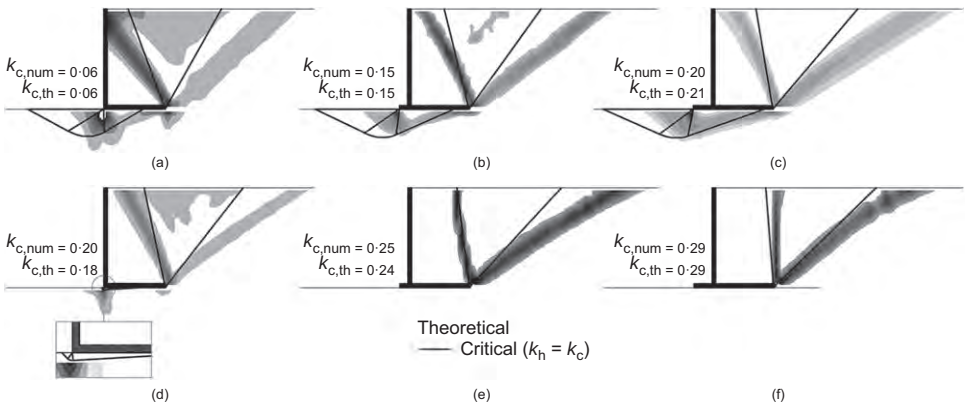

Fig. 6. Pseudostatic numerical analyses: contours of shear strains at the onset of critical conditions and comparison with the theoretical predictions: for soil profile D – (a) W1-D, (b) W2-D and (c) W3-D; for soil profile UD – (d) W1-UD, (e) W2-UD and (f) W3-UD

and then the generalised Rankine conditions apply (Kloukinas & Mylonakis, 2011).

Pseudostatic stress distribution

Figure 7 shows the horizontal stresses immediately behind the vertical stem and along the vertical plane AV (Figs 7(a) and 7(c)), together with the resulting bending moment distribution (Figs 7(b) and 7(d)), computed for the layouts W3-D and W3-UD. The numerical results refer to three values of the pseudostatic coefficient ($k_h = 0$, $0{\cdot}1$, k_c). The corresponding theoretical distributions S2(k_h) and $S^{KM}_{AE,h}(k_h)$ are also shown for comparison. Starting from the static condition ($k_h = 0$) and moving to the critical one ($k_h = k_c$), the horizontal stresses increase linearly with depth, both behind the stem and along the AV plane. Moreover, the fairly good agreement between the numerical values and S2(k_h) indicates that, for both wall layouts, the soil behind the stem is in the active limit state and the MO solution provides a good estimate of the pseudostatic soil thrust. In other words, up to the critical condition ($k_h \leq k_c$), the horizontal stem does not alter substantially the stress distribution at the soil–wall contact.

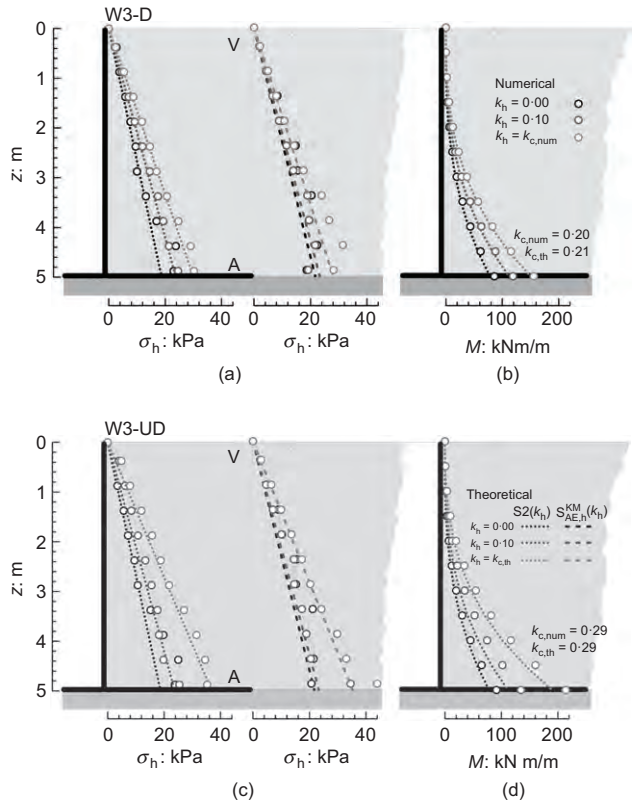

Fig. 7. Wall W3, soil profile D and UD. Numerical pseudostatic distributions of: (a), (c) horizontal stresses behind the stem and along the virtual plane AV; (b), (d) bending moments in the stem

DYNAMIC ANALYSES

Based on approximate elastic solutions (Hatami & Bathurst, 2000), a lower bound value for the fundamental frequency of the wall–backfill system can be estimated as $f_0 = V_{Sm}/H/2$ (≈ 16 Hz), where V_{Sm} is the mean shear wave velocity within the backfill. Comparing f_0 with f_m, no resonance effects are expected to occur during the dynamic inputs and essentially pseudostatic conditions apply (Nadim & Whitman, 1983). This is in agreement also with the experimental findings by Kloukinas *et al*. (2015).

Wavelet input signals

In order to clarify some aspects concerning the dynamic behaviour of yielding cantilever walls, the focus will first be placed on the simple case of a wavelet input acceleration ($a_{max} = 0{\cdot}25\boldsymbol{g}$). The wall W3 will be used as reference, overlying both the D and UD soil profile, to highlight possible differences between the sliding (W3-UD) and bearing (W3-D) failure modes.

Figure 8 shows, for the right wall, the time histories of: free-field and wall absolute horizontal accelerations (Figs 8(a) and 8(b)); and horizontal displacements of the wall (Figs 8(c) and 8(d)). The absolute accelerations of the wall coincide with the free-field one as long as the critical value, a_c, is not exceeded. For larger values of the free-field acceleration, the wall starts to move, by either a combination of rotation and sliding (D) or pure sliding (UD). During these time intervals, the accelerations at the top and at the bottom of the stem can vary, if the wall rotates, but the acceleration at mid-height of the stem remains approximately constant and equal to a_c. As expected, even though the free-field accelerations in the two analyses are quite similar, the permanent displacements experienced by the wall differ significantly, both in magnitude and trend, as a result of the different critical mechanism characterising the drained and the undrained case.

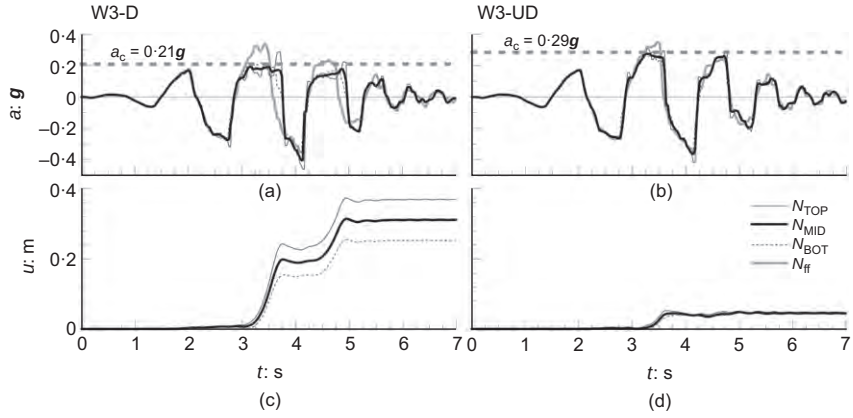

Fig. 8. Right wall W3, soil profile D and UD, input wavelet ($a_{max} = 0{\cdot}25\boldsymbol{g}$). Time histories of: (a), (b) horizontal free-field and wall accelerations; (c), (d) wall displacements

To highlight the physical significance of the critical acceleration, Fig. 9 shows the temporal evolution of the quantity $(S_{E,h} + T_E - S_{AV,h})/W_s$, computed numerically by integrating the corresponding stresses over the soil elements behind the stem ($S_{E,h}$), above the heel (T_E) and along the virtual back AV ($S_{AV,h}$). According to the force equilibrium given in Fig. 1(d), this quantity corresponds to the average normalised acceleration experienced by the soil mass above the heel. In both analyses, the critical acceleration defines the maximum (positive) acceleration that the soil–wall system can ever experience during a dynamic event. Moreover, the acceleration computed at mid-height of the stem provides a good estimate of the average acceleration experienced by the whole system.

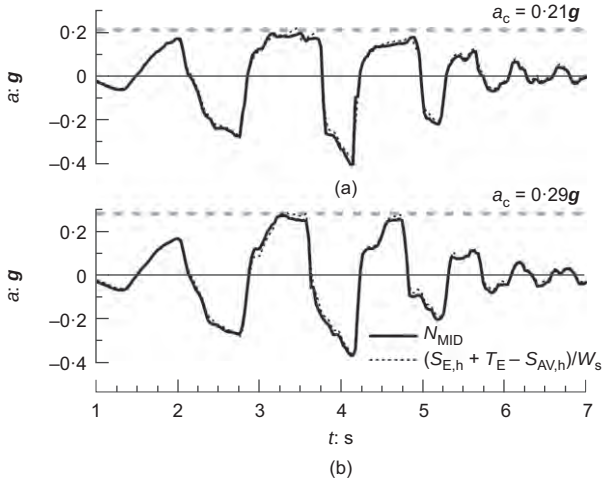

Fig. 9. Right wall W3, input wavelet (a_{max} = 0·25g). Time histories of the acceleration at mid-height of the stem and of the average acceleration into the soil–wall system for: (a) soil profile D; (b) soil profile UD

Figure 10 shows, for the right wall, the time histories of: free-field and wall absolute horizontal accelerations (Figs 10(a) and 10(b)); the total horizontal force computed in the soil elements immediately behind the vertical stem, $S_{E,h}$, and along the virtual face AV, $S_{AV,h}$ (Figs 10(c) and 10(d)); and the bending moment at the base of the stem (Figs 10(e) and 10(f)). Fig. 10 also reports the horizontal soil thrust (Figs 10(c) and 10(d)) and the maximum bending moment (Figs 10(e) and 10(f)) predicted by the two approximate solutions S1($k_h = k_c$) and S2($k_h = k_c$) (critical condition). Finally, Figs 10(c) and 10(d) show the horizontal soil thrust predicted by limit analysis for $k_h = k_c$, $S^{KM}_{AE,h}(k_c)$. The numerical results of $S_{AV,h}$ and $S_{E,h}$ exhibit a completely different behaviour. On the one hand, $S_{AV,h}$ increases when the inertia forces in the system are directed towards the backfill and decreases when they are directed away from the backfill, reaching its minimum in the time intervals when the wall moves relative to the surrounding soil. The minimum values of $S_{AV,h}$, corresponding to an active limit condition into the soil, are in good agreement with $S^{KM}_{AE,h}(k_c)$. On the other hand, $S_{E,h}$ reaches its maximum under positive (rightwards) accelerations, that is when the inertia forces into the soil–wall system are directed away from the backfill. This result, in apparent contradiction of what has been observed for gravity retaining walls (Athanasopoulos-Zekkos *et al.*, 2013; Conti *et al.*, 2013), stems from the fact that S_E, being an internal force between the wall and the backfill, depends on the masses W_w/g and W_s/g. It follows that, where cantilever walls are concerned (W_w significantly smaller than W_s), S_E is always maximised when the backfill is

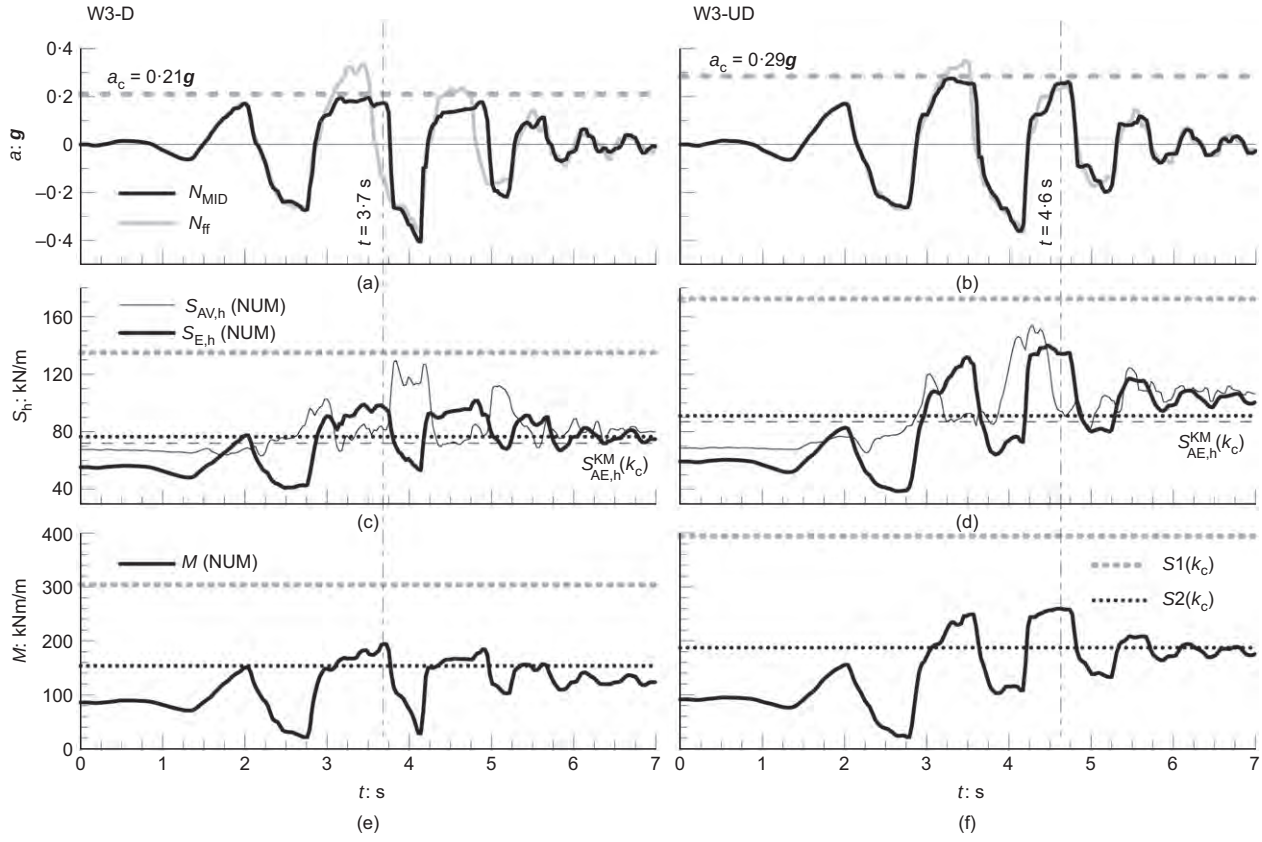

Fig. 10. Right wall W3, soil profile D and UD, input wavelet (a_{max} = 0·25g). Time histories of: (a), (b) horizontal free-field and wall accelerations; (c), (d) horizontal soil thrust behind the stem and at the virtual plane AV; (e), (f) bending moment at the base of the stem

'pushing' towards the wall (rightwards accelerations). The maximum value of $S_{E,h}$ depends on the amount of shear stress transferred through the internal heel, T_E, which is related to the shear deformations at the contact between the heel and the soil above it and which could hardly be predicted within a perfect plasticity framework.

Moving to the bending moments (Figs 10(e) and 10(f)), their maximum value, M_{max}, occurs together with the maximum soil thrust behind the stem, that is when the inertia forces are directed away from the backfill and the wall is moving relative to the soil. Comparing the numerical results with the approximate solutions S1(k_c) and S2(k_c), in terms of both horizontal soil thrust and bending moment, it is clear that S1(k_c) provides always a physical upper bound for their maximum values, whereas S2(k_c) can lead to even a gross underestimation. This observation implies that, when the wall is moving, the presence of the horizontal heel does affect the horizontal stress distribution behind the vertical stem.

A further representation of the observed behaviour is given in Fig. 11, which shows, for the time instant corresponding to which the bending moment attains its maximum value, the spatial distribution of: horizontal stresses immediately behind the vertical stem (Figs 11(a) and 11(d)); bending moment in the structural element (Figs 11(b) and 11(e)); and horizontal accelerations of the wall and in free-field conditions (Figs 11(c) and 11(f)). Again, the theoretical distributions provided by the two approximate solutions are also reported for comparison. As far as the soil profile D is concerned, the numerical distributions of both the contact stresses and the bending moment are bounded between the two theoretical solutions, thus suggesting that T_E is participating in the overall equilibrium of the soil mass above the heel. The (rightwards) accelerations on the wall are not constant due to the ongoing rotation, but with an average value approximately equal to the critical one, and are out of phase with respect to the (leftwards) free-field accelerations. As far as the soil profile UD is concerned, the same trend is observed in terms of stress and bending moment distributions. However, in this case the accelerations on the wall are approximately constant and equal to a_c, as a result of the sliding mechanism, and no phase shift occurs with the free-field accelerations.

In order to gain a more comprehensive insight into the overall system's behaviour, Fig. 12 summarises the most relevant results also for the L-shaped walls (W1-D and W1-UD), subjected to a wavelet acceleration with $a_{max} = 0{\cdot}15\boldsymbol{g}$. Specifically, Fig. 12 shows the time histories of: horizontal free-field and wall accelerations (Figs 12(a) and 12(b)); wall displacements (Figs 12(c) and 12(d)); horizontal soil thrusts $S_{AV,h}$ and $S_{E,h}$ (Figs 12(e) and 12(f)); and bending moments on the vertical stem (Figs 12(g) and 12(h)). Being the most rotational-sensitive case, layout W1-D experiences large rotations, corresponding to which a marked phase shift is observed between free-field and wall accelerations. However, the overall behaviour is qualitatively similar to what is observed for the W3 layouts, thus confirming that the ongoing plastic mechanism does not

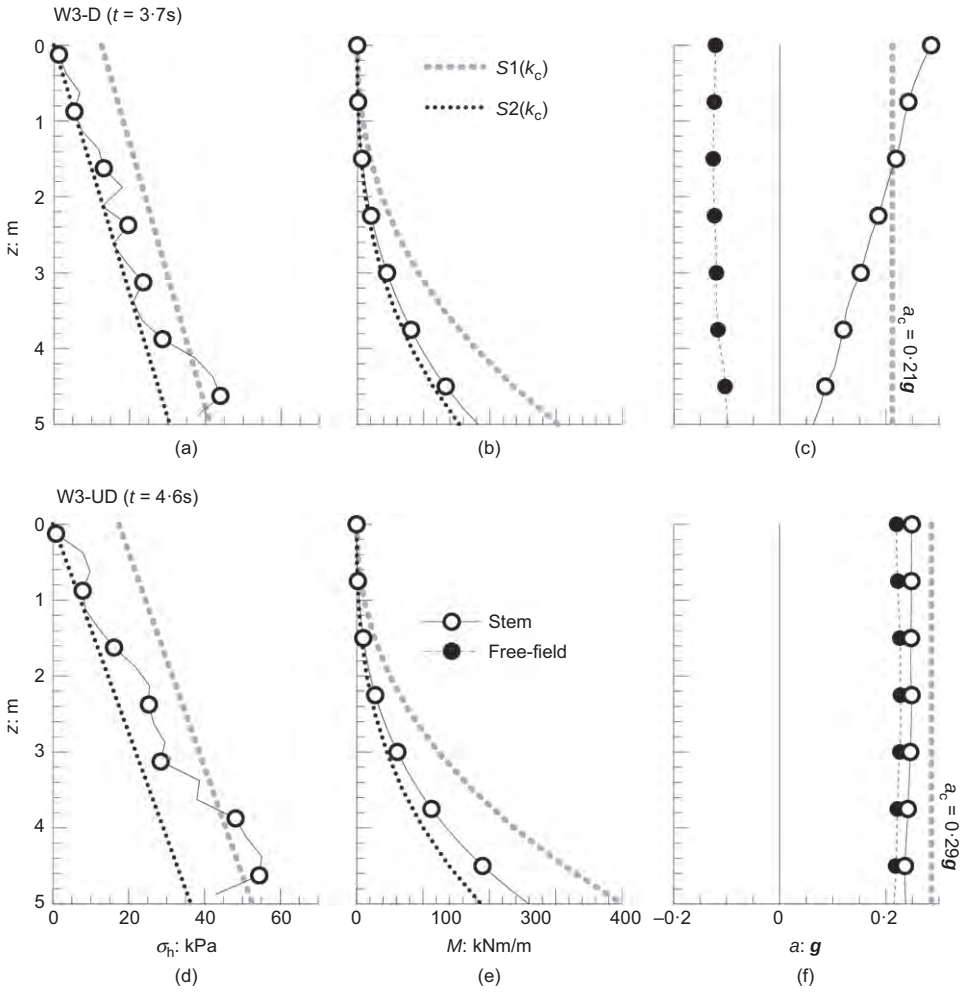

Fig. 11. Right wall W3, soil profile D and UD, input wavelet ($a_{max} = 0{\cdot}25g$). Distribution of: (a), (d) horizontal stresses behind the stem; (b), (e) structural bending moments; (c), (f) wall and free-field accelerations, at the time instant corresponding to which $M = M_{max}$

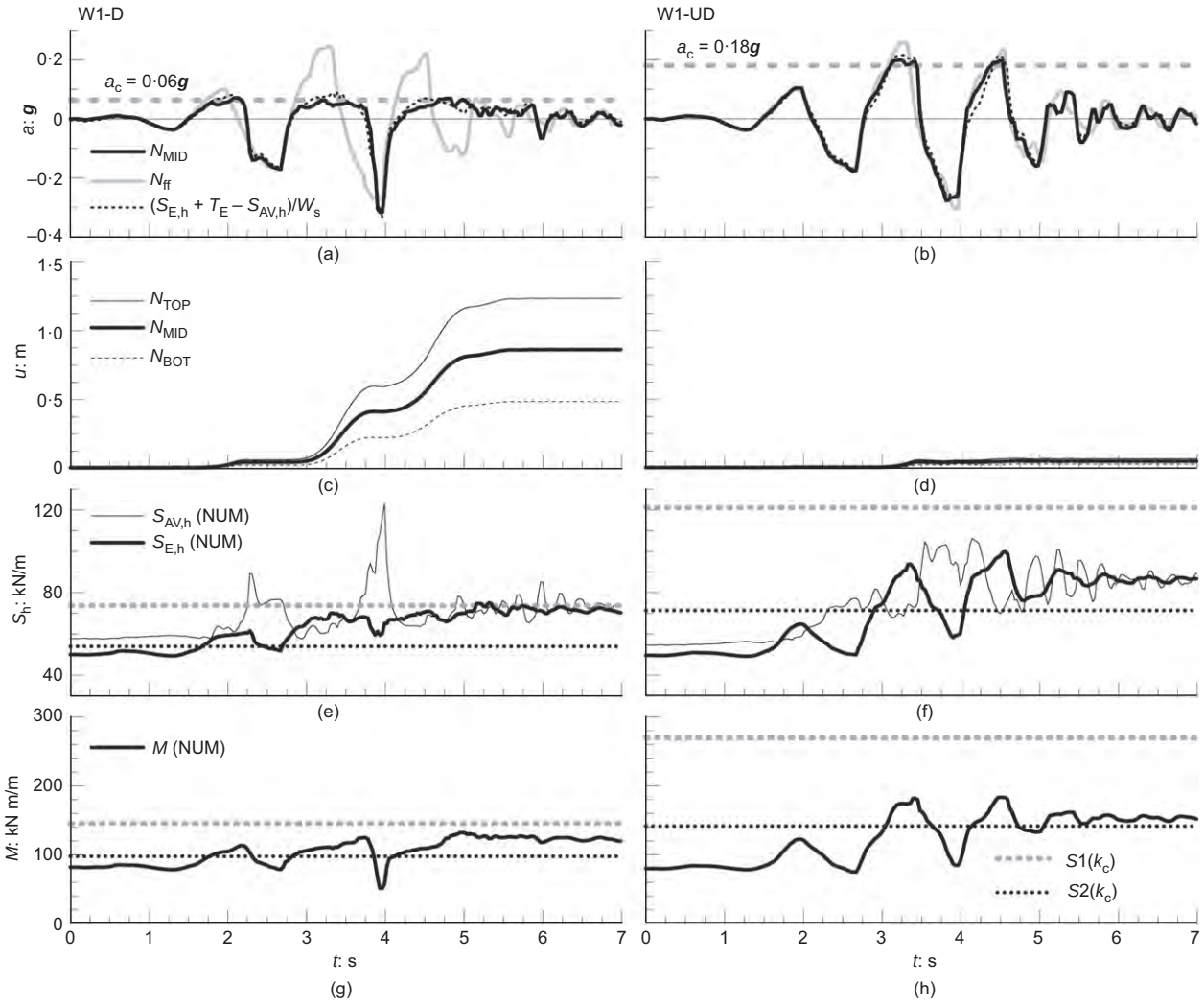

Fig. 12. Right wall W1, soil profile D and UD, input wavelet ($a_{max} = 0{\cdot}15g$). Time histories of: (a), (b) horizontal free-field, wall and system's average accelerations; (c), (d) wall displacements; (e), (f) horizontal soil thrust behind the stem and at the virtual plane AV; (g), (h) bending moment at the base of the stem

affect the dynamics of the system. Specifically, when the wall moves, its average acceleration remains constant and approximately equal to a_c; the maximum soil thrust, $S_{Eh,max}$, and the maximum bending moment occur when the inertia forces into the system act in the active direction, that is away from the backfill; during wall displacements, the maximum internal forces are bounded by the two pseudostatic solutions S1(k_c) and S2(k_c).

Real input earthquakes

For the sake of conciseness, the dynamic response of cantilever walls during real earthquakes will be discussed in terms of synthetic parameters, both kinematic (wall and free-field accelerations, maximum wall displacement) and static (maximum soil thrust, maximum bending moment), usually adopted as performance indicators for the system.

Figure 13 reports the maximum acceleration computed at mid-height of the stem (N_{MID}) against the maximum free-field acceleration (N_{ff}), for the drained (Figs 13(a)) and the undrained (Figs 13(b)) analyses, together with the theoretical values of the critical acceleration. Maximum rightwards ($a_{max,MID}$, $a_{max,ff}$) and leftwards ($|a_{min,MID}|$, $|a_{min,ff}|$) accelerations are considered for the right and the left wall, respectively. As expected, once the critical threshold is attained – that is as soon as a plastic mechanism develops within the soil–wall system – the absolute acceleration of the system remains approximately constant, starting to deviate from the free-field excitation. Moreover, the theoretical predictions of a_c are in good agreement with the numerical results.

Figure 14 shows the maximum normalised values of the horizontal soil thrust, $S_{Eh,max}/\gamma H^2$, and of the structural bending moment, $M_{max}/\gamma H^3$, as a function of the maximum free-field acceleration, for the drained (Figs 14(a) and 14(c)) and the undrained (Figs 14(b) and 14(d)) analyses, respectively. The approximate solutions S1(k_h), S1(k_c) and S2(k_h) are also plotted for comparison. For a given layout, the maximum soil thrust on the stem, and hence the maximum bending moment, can increase even for $a_{max,ff} > a_c$, even though the absolute acceleration of the system remains constant, due to an internal redistribution of stresses leading to a reduction of T_E. Nonetheless, the solution S1(k_c), corresponding to $T_E = 0$, always defines the upper bound for $S_{Eh,max}$ and M_{max}. Moreover, as long as this limiting condition is not achieved, the solution S2($k_h = a_{max,ff}/g$) provides a reasonable estimate of the maximum internal forces in the stem, with a maximum relative scatter of about 20%, in terms of bending moment, with respect to the numerical values.

A key ingredient for the assessment of the seismic performance of cantilever walls is the maximum horizontal

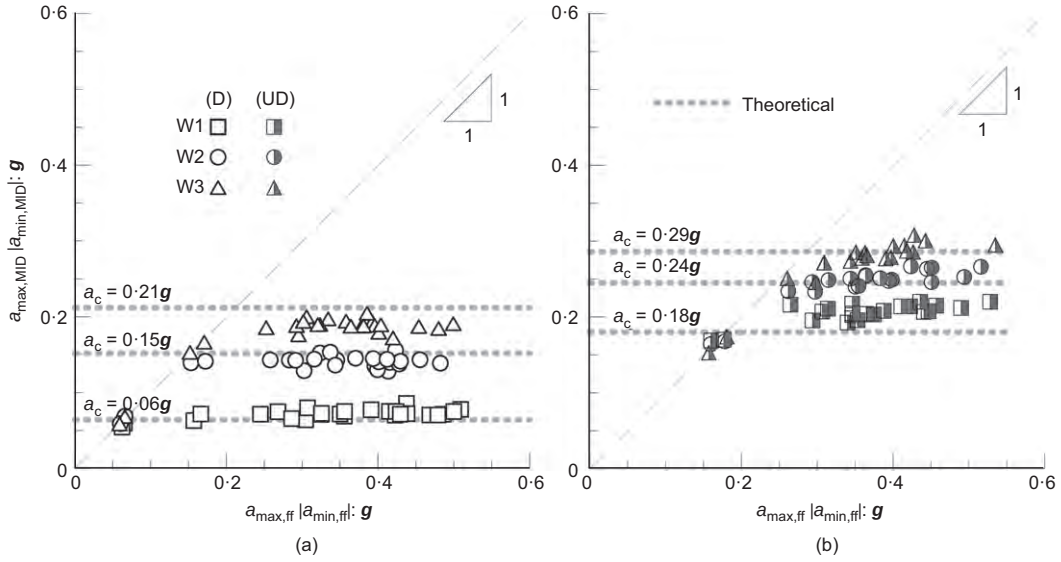

Fig. 13. Numerical dynamic analyses. Maximum horizontal accelerations of the wall (N_{MID}) as a function of the maximum free-field acceleration (N_{ff}): (a) soil profile D; (b) soil profile UD

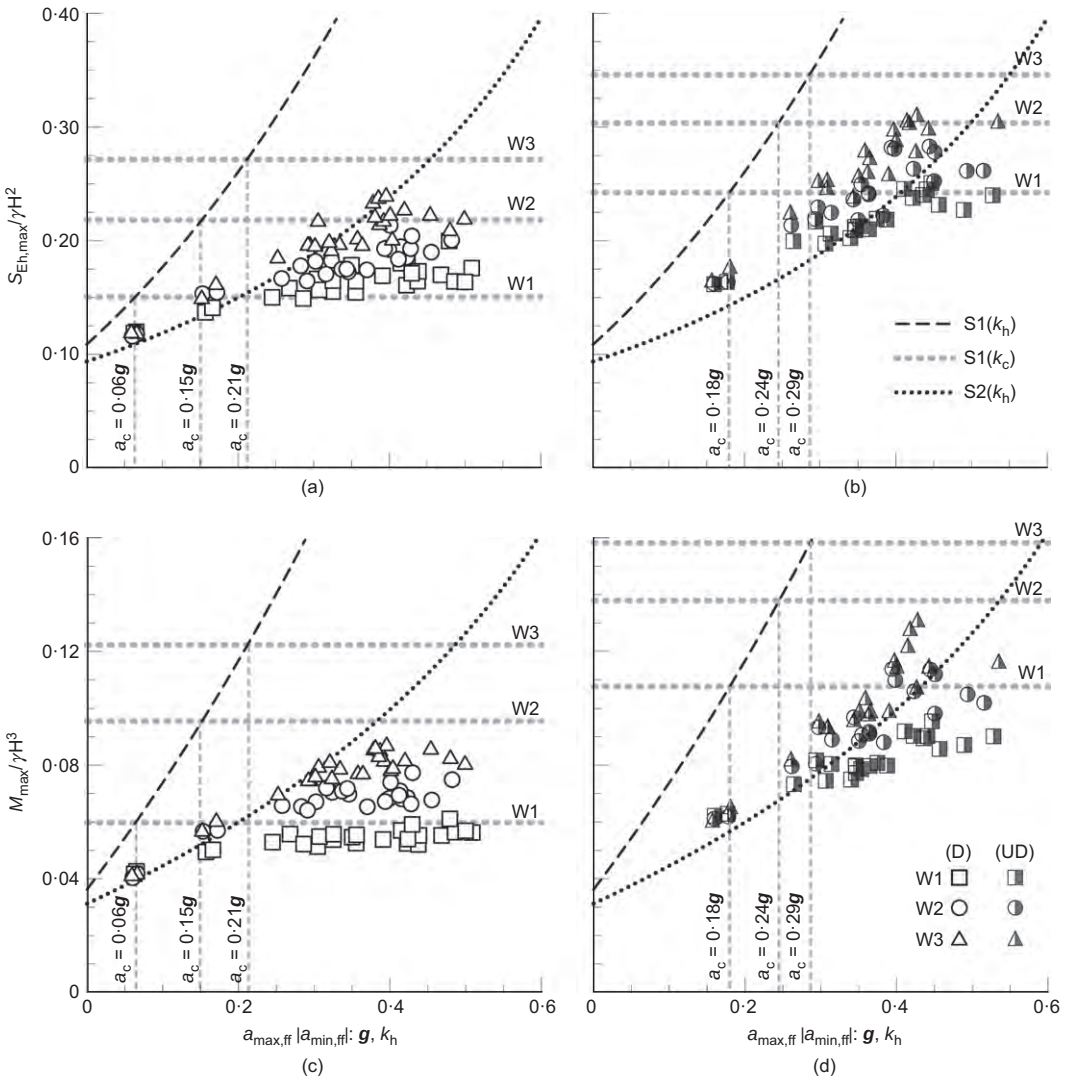

Fig. 14. Numerical dynamic analyses. Maximum soil thrust behind the stem and maximum bending moment as a function of the maximum free-field acceleration: (a), (c) soil profile D; (b), (d) soil profile UD

displacement of the vertical stem, controlling the vertical settlements in the backfill and hence the potential damage to adjacent buildings. Fig. 15 shows the final horizontal displacements of the top of the wall, u, both in dimensional (Figs 15(a)) and non-dimensional (Figs 15(b) and 15(c)) form, as a function of the ratio $a_c/a_{max,ff}$ between the (theoretical) critical acceleration and the maximum free-field acceleration. The normalised expressions

$$\bar{u} = \frac{u a_{max,ff}}{V_{max,ff}^2} \quad \text{and} \quad \bar{u} = \frac{u}{a_{max,ff} T_{m,ff} T_{5-95,ff}}$$

taking into account also the frequency content and the duration of the free-field signal, have been derived from Newmark (1965) and Ausilio *et al*. (2007), respectively, where $V_{max,ff}$ is the maximum velocity, $T_{m,ff}$ is the mean period and $T_{5\text{-}95,ff}$ is the duration of the strong motion. Fig. 15 also reports some of the interpolating functions proposed in the literature, all derived from the application of the Newmark's sliding block procedure (Newmark, 1965; Richards & Elms, 1979; Whitman & Liao, 1985; Saygili & Rathje, 2008), together with the best fit of the numerical results presented herein, obtained using the same functional form for both u and its dimensionless expressions. As expected, the computed displacements reduce with increasing the ratio $a_c/a_{max,ff}$. However, while the numerical results for the UD profile are in satisfactory agreement with the equation proposed by Richards & Elms (1979) for sliding walls, those corresponding to the D profile are always above the predictive relationships. This observation suggests that the available equations, all derived from the analysis of a rigid block sliding over a horizontal plane, can lead to non-conservative results if applied to retaining walls for which the permanent displacement stems from a combination of both sliding and rotation.

A similar conclusion can be drawn by inspection of Fig. 16, showing the final horizontal displacements computed at three points along the vertical stem (N_{BOT}, N_{MID}, N_{TOP}) against the displacements provided by a Newmark's type calculation, carried out assuming as the base input the numerical acceleration computed in free-field conditions

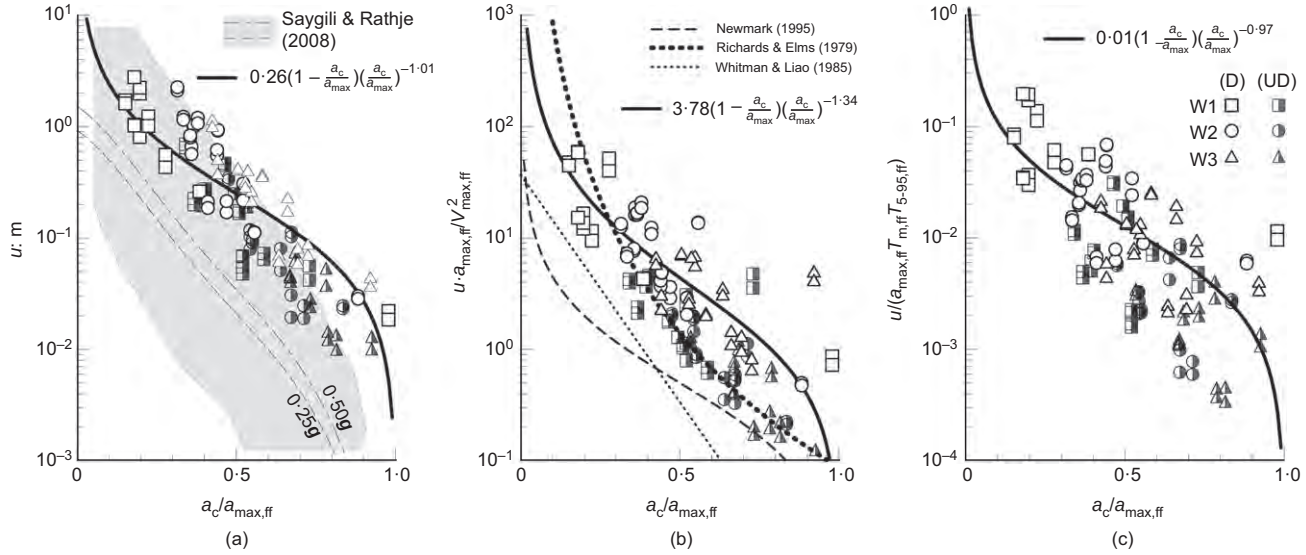

Fig. 15. Numerical dynamic analyses. Final horizontal displacement of the top of the wall (N_{TOP}) as a function of the ratio $a_c/a_{max,ff}$: (a) numerical results; (b) normalised displacements according to Newmark (1965); (c) normalised displacements according to Ausilio *et al*. (2007)

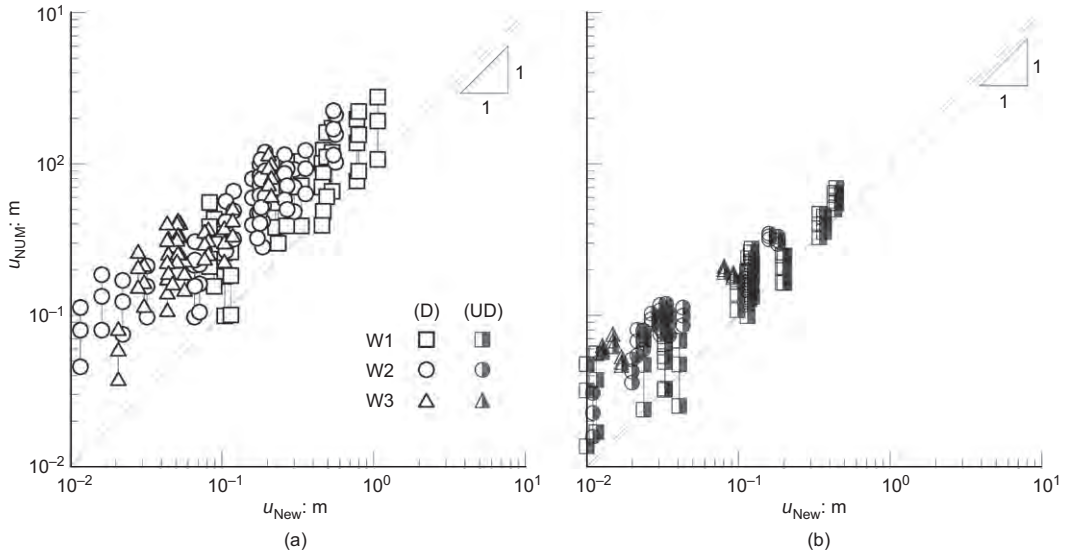

Fig. 16. Numerical dynamic analyses. Final horizontal displacement of the wall, u_{NUM} (points: N_{TOP}, N_{MID}, N_{BOT}), as a function of the displacement predicted by the Newmark's analysis, u_{New}: (a) soil profile D; (b) soil profile UD

(N_{ff}). Incidentally, note that the same results have been obtained also using the acceleration computed at node N_B, closer to the walls but still outside the active limit zone, thus indicating that no appreciable amplifications occurred close to the system. The displacements computed for the D profile (Fig. 16(a)) are significantly larger than those corresponding to the UD profile (Fig. 16(b)), and always associated to a substantial rotation of the wall. Moreover, the Newmark's calculation always under-predicts the actual average displacement for the D profile, while it is in satisfactory agreement with the numerical results for the UD profile.

DISCUSSION OF RESULTS

The main results of the dynamic analyses can be summarised as follows.

(*a*) Contrary to what is argued by other authors (Green *et al.*, 2008; Al Atik & Sitar, 2010; Kloukinas *et al.*, 2015), during a dynamic event, the maximum values of $S_{E,h}$ and of the structural bending moment are always in phase and occur when the inertia forces into the system are directed away from the backfill. An opposite trend is observed for $S_{AV,h}$, whose maxima occur when the inertia forces act towards the backfill. This latter condition, however, has no relevance in the seismic stability of the wall, either external (geotechnical design) or internal (structural design).

(*b*) Possible phase shifts can occur between free-field and wall accelerations, when the wall undergoes permanent displacements. Moreover, the actual average acceleration of the soil–wall system can differ significantly from the free-field one, its physical upper bound corresponding to the critical value a_c. Consistently, also, the maximum inertia force that the system can ever experience during an earthquake is bounded by its critical value. This observation is in substantial agreement with the experimental findings by Koseki *et al.* (2003).

(*c*) When the wall moves, the shear force T_E contributes to the equilibrium of the soil mass above the heel, thus affecting the amount of inertia force effectively transferred to the vertical stem. However, the pseudostatic solution S1(k_c) (corresponding to $T_E = 0$) always defines the ever possible upper bound for the maximum internal forces on the wall. Moreover, from a practical point of view, the solution S2($k_h = a_{max,ff}/\boldsymbol{g}$) provides a reasonable prediction of both the maximum soil thrust on the stem and the maximum bending moment, provided the limiting value S1(k_c) is not achieved.

In the light of points (*a*) and (*b*) above, close attention must be paid when interpreting the dynamic behaviour of yielding cantilever walls using only the free-field acceleration as reference, since the free-field motion does not necessarily correspond to the acceleration actually experienced by the system. This evidence makes it possible to explain the apparent mismatch between the numerical results presented so far and some of the experimental and field observations reported in the literature (Mikola *et al.*, 2016; Wagner & Sitar, 2016) – leading to the main practical conclusion that the MO solution overestimates significantly the dynamic soil thrust at large free-field accelerations ($a_{max,ff} > 0{\cdot}4\boldsymbol{g}$). Indeed, for such large values of the free-field acceleration, it is likely that the wall has already attained its critical condition. In other words, when applying limit equilibrium or plasticity solutions, the pseudostatic coefficient cannot be linked, in principle, to the free-field acceleration, but rather to the actual acceleration of the yielding system.

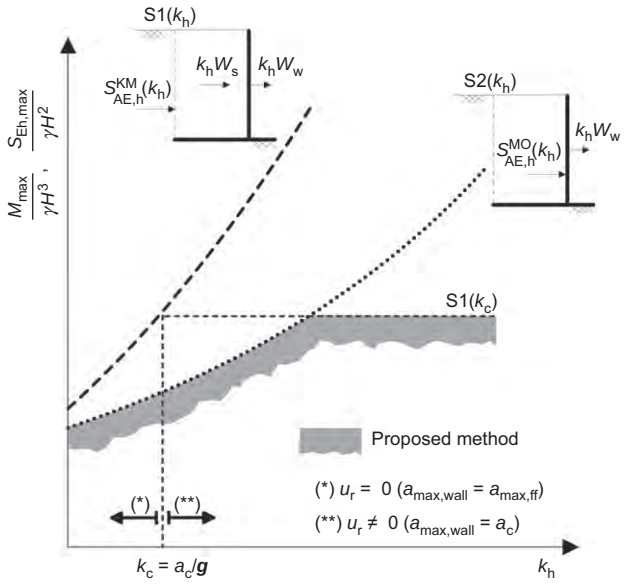

Fig. 17. Pseudostatic method for computing the maximum soil thrust and internal forces in yielding cantilever walls (structural design)

Consistently with the above results, a simple three-step procedure for the structural design of yielding cantilever retaining walls can be defined, taking into account, although approximately, the possible contribution of the horizontal stem to the overall dynamic equilibrium. As summarised in Fig. 17: (*a*) compute the critical acceleration of the wall; (*b*) use S1(k_c) to compute the maximum internal forces that the wall could ever experience during an earthquake; (*c*) for a given design earthquake, corresponding to which $k_h = a_{max,ff}/\boldsymbol{g}$, use S2($k_h$) to compute the internal forces in the wall, as long as S2(k_h) < S1(k_c), otherwise use S1(k_c).

CONCLUSIONS

The numerical results presented in this paper made it possible both to gain valuable information on the seismic behaviour of yielding cantilever walls, in terms of expected permanent displacements and maximum internal forces, and to validate the predictions of a simple pseudostatic model, based on limit equilibrium/analysis methods.

As already observed for other types of yielding retaining structures (Conti *et al.*, 2013, 2014), the dynamic behaviour of cantilever walls is primarily governed by the strength of the system, while the wall flexibility and the soil stiffness play a minor role. A direct consequence of this observation is that the critical acceleration turns out to be the key ingredient for their seismic design, controlling both the maximum structural internal forces and the final displacement.

The critical acceleration and the magnitude and trend of the final displacements depend on the plastic mechanism actually activated during the earthquake. Sliding and bearing failure are both ductile mechanisms for the system, inducing a progressive accumulation of permanent displacements during shaking. As a matter of fact, contrary to a pure overturning failure mechanism, the temporary mobilisation of the soil shear resistance beneath the foundation would not lead to a fragile collapse of the system, provided that an excessive wall tilting is prevented. A performance-based (and more economic) design of cantilever walls should then contemplate the possible activation of both mechanisms,

depending on the particular wall geometry and soil condition, instead of excluding a priori the expected rotation.

On the other hand, the results of the current study have shown that a direct application of Newmark's sliding block procedure to critical mechanisms involving a bearing failure of the foundation can lead to a significant under-prediction of the final displacement. Further research is therefore required to develop reliable theoretical models, capable of handling combined tilting and sliding failure modes.

As far as the structural design of the wall is concerned, numerical results have pointed out, on the one hand, that no phase shift occurs between the maximum soil thrust on the vertical stem, its maximum bending moment and the inertia forces into the wall–backfill system. On the other hand, when the wall is moving, the presence of the horizontal heel can affect the inertia force effectively transferred to the vertical stem, leading to a possible increase of bending moment under a constant absolute acceleration. In this case, an approximate procedure to handle the structural design of the wall has been proposed, combining the predictions of two simple pseudostatic plasticity solutions.

ACKNOWLEDGEMENT

The work presented in this paper was developed with the financial support of the Italian Department of Civil Protection within the ReLUIS research project.

APPENDIX

Using the lower bound theorem of limit analysis, Kloukinas & Mylonakis (2011) and Evangelista *et al.* (2010) derived the expression for the dynamic active soil thrust acting on the vertical plane AV (see Fig. 1)

$$S_{AE} = \frac{1}{2}\gamma K_{AE} H^2 \tag{1}$$

where the dynamic active earth pressure coefficient, K_{AE}, is given by

$$K_{AE} = \frac{\cos\varepsilon\cos(\varepsilon+\psi)}{\cos\delta_S\cos\psi}\left[\frac{1-\sin\phi\cos(\Delta_{1e}-\varepsilon+\psi)}{1+\sin\phi\cos(\Delta_{1e}+\varepsilon+\psi)}\right] \tag{2}$$

in which

$$\psi = \operatorname{atan}\left(\frac{a_h}{1-a_v}\right), \quad \sin\Delta_{1e} = \frac{\sin(\varepsilon+\psi)}{\sin\phi}$$

ε is the slope of the backfill and δ_S is the inclination of the soil thrust on the horizontal

$$\delta_S = \operatorname{atan}\left[\frac{\sin\phi\sin(\Delta_{1e}-\varepsilon+\psi)}{1+\sin\phi\cos(\Delta_{1e}-\varepsilon+\psi)}\right] \tag{3}$$

Finally, the angles of inclination of the two failure surfaces on the vertical direction are given by

$$\omega_\beta = \frac{\pi}{4} - \frac{\phi}{2} - \frac{(\Delta_{1e}-\varepsilon)}{2} - \frac{\psi}{2}, \quad \omega_\alpha = \frac{\pi}{2} - \phi - \omega_\beta \tag{4}$$

NOTATION

a_c	critical acceleration
a_h	horizontal acceleration
$a_{max,ff}$	maximum free-field acceleration
a_v	vertical acceleration
$a_{y,SLID}$	yielding acceleration for sliding over the base
$a_{y,QLIM}$	yielding acceleration for bearing capacity failure of the foundation soil
d	width of wall heel
H	wall height
$K_{AE,h}^{KM}$	earth pressure coefficient (generalised Rankine solution)
$K_{AE,h}^{MO}$	earth pressure coefficient (MO solution)
k_h	horizontal pseudostatic coefficient
M_{max}	maximum bending moment
$S_{AE,h}^{KM}$	horizontal soil thrust (generalised Rankine solution)
$S_{AE,h}^{MO}$	horizontal soil thrust (MO solution)
$S_{E,h}$	horizontal soil thrust on the vertical stem
SF_{QLIM}	static global safety factor for bearing capacity failure of the foundation soil
SF_{SLID}	static global safety factor for sliding over the base
u	horizontal displacement
W_s	weight of the soil volume above the wall heel
$W_{w,stem}$	weight of the wall stem
z	depth
γ	unit weight of the backfill
δ_s	inclination of the soil thrust on the horizontal (generalised Rankine solution)
ε	slope of the backfill
σ_h	horizontal stress
ϕ'	soil friction angle
ω_α	inclination of the α-characteristic (generalised Rankine solution)
ω_β	inclination of the β-characteristic (generalised Rankine solution)

REFERENCES

Aashto (American Association of State Highway and Transportation Officials) (2012). *LRFD bridge design specifications*, 6th edn. Washington, DC, USA: Aashto.

Al Atik, L. & Sitar, N. (2010). Seismic earth pressures on cantilever retaining structures. *J. Geotech. Geoenviron. Engng* **136**, No. 10, 1324–1333.

Anderson, D. G., Martin, G. R., Lam, I. & Wang, J. N. (2008). *Seismic analysis and design of retaining walls, buried structures, slopes, and embankments*, NCHRP Rep. 611. Washington, DC, USA: Transportation Research Board.

Athanasopoulos-Zekkos, A., Vlachakis, V. S. & Athanasopoulos, G. A. (2013). Phasing issues in the seismic response of yielding, gravity-type earth retaining walls – overview and results from a FEM study. *Soil Dynamics Earthquake Engng* **55**, 59–70.

Ausilio, E., Silvestri, F. & Tropeano, G. (2007). Simplified relationships for estimating seismic slope stability. *Proceedings of the ISSMGE–ETC12 workshop on geotechnical aspects of EC8*, Madrid, Spain.

Brandenberg, S. J., Mylonakis, G. & Stewart, J. P. (2015). Kinematic framework for evaluating seismic earth pressures on retaining walls. *J. Geotech. Geoenviron. Engng* **141**, No. 7, 04015031.

Conti, R. (2018). Simplified formulas for the seismic bearing capacity of shallow strip foundations. *Soil Dynamics Earthquake Engng* **104**, 64–74.

Conti, R., Madabhushi, S. P. G. & Viggiani, G. M. B. (2012). On the behaviour of flexible retaining walls under seismic actions. *Géotechnique* **62**, No. 12, 1081–1094, https://doi.org/10.1680/geot.11.P.029.

Conti, R., Viggiani, G. M. B. & Cavallo, S. (2013). A two-rigid block model for sliding gravity retaining walls. *Soil Dynamics Earthquake Engng* **55**, 33–43.

Conti, R., Viggiani, G. M. B. & Burali d'Arezzo, F. (2014). Some remarks on the seismic behaviour of embedded cantilevered retaining walls. *Géotechnique* **64**, No. 1, 40–50, https://doi.org/10.1680/geot.13.P.031.

Evangelista, A., Scotto di Santolo, A. & Simonelli, A. L. (2010). Evaluation of pseudostatic active earth pressure coefficient of cantilever retaining walls. *Soil Dynamics Earthquake Engng* **30**, No. 11, 1119–1128.

Gazetas, G., Garini, E., Anastasopoulos, I. & Georgarakos, T. (2009). Effects of near-fault ground shaking on sliding systems. *J. Geotech. Geoenviron. Engng* **135**, No. 12, 1906–1921.

Green, R. A., Olgun, C. G. & Cameron, W. I. (2008). Response and modelling of cantilever retaining walls subjected to seismic motions. *Comput.-aided Civil Infrastruct. Engng* **23**, No. 4, 309–322.

Hatami, K. & Bathurst, R. J. (2000). Effect of structural design on fundamental frequency of reinforced-soil retaining walls. *Soil Dynamics Earthquake Engng* **19**, No. 3, 137–157.

Itasca (2005). *FLAC fast Lagrangian analysis of continua, v. 5.0. User's manual*. Minneapolis, MN, USA: Itasca.

Kloukinas, P. & Mylonakis, G. (2011). Rankine solution for seismic earth pressures on L-shaped retaining walls. *Proceedings of the 5th international conference on earthquake geotechnical engineering (5ICEGE)*, Santiago, Chile.

Kloukinas, P., Scotto di Santolo, A., Penna, A., Dietz, M., Evangelista, A., Simonelli, A. L., Taylor, C. & Mylonakis, G. (2015). Investigation of seismic response of cantilever retaining walls: limit analysis vs shaking table testing. *Soil Dynamics Earthquake Engng* **77**, 432–445.

Koseki, J., Tatsuoka, F., Watanabe, K., Tateyama, M., Kojima, K. & Munaf, Y. (2003). Model tests of seismic stability of several types of soil retaining walls. In *Reinforced soil engineering: advances in research and practice* (eds H. I. Ling, D. Leshchinsky and F. Tatsuoka), pp. 317–358. New York, NY, USA: Marcel Dekker.

Masini, L., Callisto, L. & Rampello, S. (2015). An interpretation of the seismic behaviour of reinforced-earth retaining structures. *Géotechnique* **65**, No. 5, 349–358, https://doi.org/10.1680/geot.SIP.15.P.001.

Mikola, R. G., Candia, G. & Sitar, N. (2016). Seismic earth pressures on retaining structures and basement walls in cohesionless soils. *J. Geotech. Geoenviron. Engng* **142**, No. 10, 04016047.

Nadim, F. & Whitman, R. V. (1983). Seismically induced movement of retaining walls. *J. Geotech. Engng* **109**, No. 7, 915–931.

Newmark, N. M. (1965). Effects of earthquakes on dams and embankments. *Géotechnique* **15**, No. 2, 139–160, https://doi.org/10.1680/geot.1965.15.2.139.

Psarropoulos, P. N., Klonaris, G. & Gazetas, G. (2005). Seismic earth pressures on rigid and flexible retaining walls. *Soil Dynamics Earthquake Engng* **25**, No. 7–10, 795–809.

Richards, R. & Elms, D. G. (1979). Seismic behaviour of gravity retaining walls. *J. Geotech. Engng Div., ASCE* **105**, No. 4, 449–464.

Saygili, G. & Rathje, E. M. (2008). Empirical predictive models for earthquake-induced sliding displacements of slopes. *J. Geotech. Geoenviron. Engng* **134**, No. 6, 790–803.

Seed, H. B. & Sun, J. I. (1989). *Implication of site effects in the Mexico City earthquake of September 19, 1985 for earthquake-resistant design criteria in the San Francisco Bay area of California*, Report UCB/EERC-89/03. Berkeley, CA, USA: Earthquake Engineering Research Center, University of California.

Veletsos, A. S. & Younan, A. H. (1997). Dynamic response of cantilever retaining walls. *J. Geotech. Geoenviron. Engng* **123**, No. 2, 161–172.

Verdugo, R., Sitar, N., Frost, J. D., Bray, J. D., Candia, G., Eldridge, T., Hashash, Y., Olson, S. & Urzua, A. (2012). Seismic performance of earth structures during the February 2010 Maule, Chile, earthquake: dams, levees, tailings dams, and retaining walls. *Earthquake Spectra* **28**, No. S1, S75–S96.

Vucetic, M. & Dobry, R. (1991). Effect of soil plasticity on cyclic response. *J. Geotech. Geoenv. Engng* **117**, No. 1, 89–107.

Wagner, N. & Sitar, N. (2016). On seismic response of stiff and flexible retaining structures. *Soil Dynamics Earthquake Engng* **91**, 284–293, https://doi.org/10.1016/j.soildyn.2016.09.025.

Whitman, R. V. & Liao, S. (1985). *Seismic design of retaining walls*, Miscellaneous Paper GL-85-1. Vicksburg, MS, USA: U.S. Army Engineer Waterways Experiment Station.